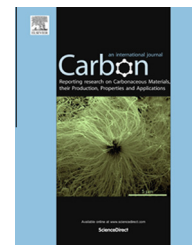


Available at www.sciencedirect.com

ScienceDirect

journal homepage: www.elsevier.com/locate/carbon

Role of residual polymer on chemical vapor grown graphene by Raman spectroscopy



Eunhye Koo, Sang-Yong Ju *

Department of Chemistry, Yonsei University, Seoul 120-749, Republic of Korea

ARTICLE INFO

Article history:

Received 4 December 2014

Accepted 28 January 2015

Available online 7 February 2015

ABSTRACT

Although various applications extensively utilize polymer-assisted graphene transfer step, the role of residual polymer on graphene was not well-understood. Here, we report the effect of poly (methyl methacrylate) (PMMA) on chemical vapor deposition-grown hexagonal graphene via Raman spectroscopy. Analysis of bare-, PMMA-covered supported, and PMMA-covered suspended graphene exhibits that their G and 2D band positions are progressively downshifted in that order. Mapping of spatial G and 2D band shifts into doping and strain contributions shows that PMMA residue exerts moderate 0.15% tensile strain on graphene/substrate, as compared to that of bare graphene. During this tensile strain, residual PMMA-covered graphene maintains its doping level as much as bare graphene does.

© 2015 Elsevier Ltd. All rights reserved.

1. Introduction

Graphene, a one-atom-thick honeycomb lattice of sp^2 hybridized carbon, has gathered immense attention due to its exceptional electrical [1–3], mechanical [4], and optical properties [5]. Its two-dimensional physico-chemical property allows for versatile application in areas such as transparent protective coatings [6,7], barrier films, and membranes [8,9]. Graphene has been prepared using various methods since it was first isolated via mechanical exfoliation [10]: these include chemical vapor deposition (CVD) using metal (nickel [11], and copper [12]), SiC [13], and chemical exfoliation [14–17]. Among those methods the CVD process provides opportunity for large-area graphene as well as layer control [8,12], which result in excellent electrical [18] and mechanical [19] properties comparable to those of pristine exfoliated graphene.

Graphene transfer on a desired silicon substrate utilizes protective polymer layer such as poly (methyl methacrylate) (PMMA) for various applications [8,11,20,21]. The PMMA

residue is known to affect electrical properties of graphene [22] and the complete removal of PMMA has proven difficult [23]. Therefore, the understanding of graphene in the presence of residual PMMA has a paramount importance. For this matter, Raman spectroscopy is a powerful tool to decipher this effect. Up to now, graphene containing residual PMMA exhibits *p*-doping behavior upon electrical measurement [24]: graphene with residual PMMA on substrate appears to have upshifted G band and, upon thermal annealing, PMMA-removed graphene has further upshifted G band from that (1581 cm^{-1}) of charge-neutral monolayer graphene [25]. However, thermal annealing of graphene enhances its *p*-doping and complicates to interpret the role of residual PMMA. Recently, it has been shown that doping and strain on graphene with underlying SiO_2/Si substrate have different trajectories of G and 2D band positions (ω_G and ω_{2D} , respectively) from charge-neutral graphene, showing that *p*- or *n*-doping has much slower $\Delta\omega_{2D}/\Delta\omega_{2D}$ slope than strain does [26]. This method allows us to probe accurate description of the residual PMMA role on graphene. In this study,

* Corresponding author.

E-mail address: syju@yonsei.ac.kr (S.-Y. Ju).<http://dx.doi.org/10.1016/j.carbon.2015.01.055>

0008-6223/© 2015 Elsevier Ltd. All rights reserved.

we show that residual PMMA exerts mild tensile strain on transferred CVD-grown graphene on substrate, probed by Raman spectroscopy without any thermal treatment.

2. Experimental

2.1. Materials and instrumentations

All reagents are spectroscopic grade and used without further purification. PMMA (molecular weight: 950 kDa, 2% dilution in anisole (A2)) was purchased from MicroChem. Millipore quality deionized water with resistivity greater than 18 M Ω was used for all experiments. Silicon substrates with 285-nm thick SiO₂ (Lot#:7400383-603-Z, degenerately *p*-doped, resistivity = 1–10 Ω -cm, Shinetsu, Japan) were subject to Piranha (H₂SO₄: H₂O₂ = 7:3) cleaning for 10 min and were washed with copious amounts of water and dried with N₂. Prior to use, the substrates were stored in deionized water. CVD setup was custom-made (see Fig. S1 in the Supplementary data (SD) for the detailed setup). A pre-patterned marker and well were obtained via conventional lithography techniques (see SD for the detailed procedure). SEM images were acquired with JEOL-6701F, with an acceleration voltage of 3 keV. FT-IR spectra were collected using Vertex70 (Bruker), equipped with a DLATGS detector. The graphene-containing sample and spin-coated PMMA on a Si substrate were placed into the beam bath, and the FT-IR spectra were acquired by accumulating 100 times. A control sample was also prepared by spin-coating the PMMA solution on the Si substrate at 3000 rpm for 60 s to produce a 75-nm thick layer. Atomic force microscopy (AFM) was measured using JPK nanowizard via tapping mode. A silicon cantilever (force constant: 37 N/m, ACTA-20, App Nano) was utilized with resonance frequency at 300 kHz.

2.2. CVD growth of graphene

Graphene was grown using a custom-made low pressure CVD (LP-CVD) setup. A copper strip (0.5 \times 4 cm², purity >99.96%, Cu-113213, Nilaco Corp.) was initially dipped into acetic acid for 10 min to remove oxide layer. The Cu foil was washed with isopropanol and dried under an N₂ stream (99.99%). The dried copper strip was immediately placed in the hot zone of a fused silica tube 1 inch in diameter, and 60 standard cubic centimeters (sccm) of H₂ gas (99.9999%) was flowed onto the copper foil in the tube up to 1000 °C. Once the temperature reached 1000 °C, a mixture of 1 sccm CH₄ (99.95%, Donga Gas) and 60 sccm H₂ was continuously flowed for 80 min at the same temperature. Following the CVD growth of graphene, the stream of 60 sccm of H₂ was maintained while the sample was slowly cooled to 230 °C at a rate of \sim 25 °C/min. This method corresponds to the samples in Figs. 1 and 3. Alternatively, when partial graphene overgrows, we reduced flow speed by half for 60 min at 980 °C, corresponding to the samples in Fig. 2. In order to visualize the graphene layer, the graphene-grown copper sample was optionally oxidized at \sim 165 °C for 6 min on a hot plate in an ambient atmosphere [27].

2.3. Graphene transfer onto a SiO₂/Si substrate

The process of transferring graphene onto a desired substrate follows that of previously-reported literature [8]. PMMA was spin coated at 3000 rpm for 60 s onto a graphene-grown Cu foil as a supporting layer. Following the optional oxidation, the underlying copper foil was removed via submersion in a 0.1 M ammonium persulfate solution for 3 h, and the floating graphene with the PMMA layer was scooped out with a clean slide glass and subsequently washed with deionized water twice. The copper-removed, PMMA-supported graphene was gently transferred to a slightly-tilted Si substrate with a 285-nm thick SiO₂ layer. After drying, the sample was further dried in a vacuum oven under 30 mmHg at room temperature. The protective PMMA layer was removed via dipping into an acetone bath overnight. The substrate was gently treated with sequential acetone and isopropanol washing, and was finally dried with an N₂ stream.

2.4. Optical/contrast measurement

An optical measurement was conducted using a backscattering geometry via either 20 \times (numerical aperture (NA): 0.40, Olympus) or 100 \times (NA: 0.90, Olympus) objective lenses. Either a CMOS camera (3.6 μ m/pixel, 1280 \times 1024, DCC1645C, Thorlabs) or a Si charge-coupled device (CCD) (6.45 μ m/pixel, 1392 \times 1040, CoolSNAP HQ², Photometrics) with optional 550 nm Band pass filter (FWHM = 10 nm, FB550-10, Thorlabs) to the emission path were used to measure relative and quantitative contrast, respectively.

2.5. Raman measurements

Micro-Raman spectroscopy was constructed using a home-built upright microscope (BX-50, Olympus) as shown in Fig. S2A, according to previous literature [28]. The slit of a spectrometer (Triax320, 1800 gratings/mm, Horiba Jobin-Yvon, see Fig. S2B spectrometer efficiency according to polarization direction) with a Si array CCD (Symphony, 26 μ m/pixel, 1024 \times 256, CCD-1024 \times 256-BIDD-STE, Horiba Jobin-Yvon) was placed at the focal length (\sim 180 mm) of a tube lens in a trinocular piece (U-TR30, F.N.: 22, Olympus). A diode-pumped solid state laser (532 nm, maximum power = 2 W) was used as an excitation light source, which produces vertically-polarized beam after passing consecutive a laser cleaning filter (LL01-532-12.5, Semrock) and a Glan-Taylor polarizer (GT5, Thorlabs). Objective lenses with 50 \times (Mplan, NA = 0.75, Olympus), and 100 \times (Mplan, NA = 0.90, Olympus) were used to focus and form a diffraction-limited spot. A combination of two-stacked trinocular intermediates (U-TRU, Olympus) installed with two desired filter sets further controlled the switch between the Raman analysis and the optical imaging: the bottom intermediate has two cubes containing a dichroic long-band pass filter (LPD01-532RU-25 \times 36 \times 1.1, Chroma) and a 50/50 beam splitter. The top intermediate has a 50/50 beam splitter and long-band pass filter (LP03-532RE-25, Chroma) with a side port connected to an external collimated LED light source (white light, M625L3-L1, Thorlabs). For wide-field Raman measurement, an optional

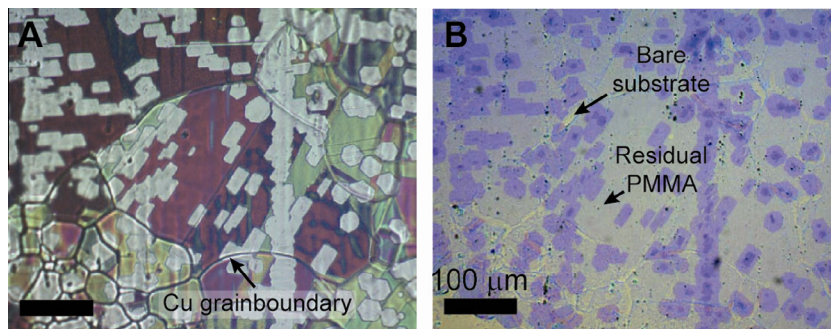


Fig. 1 – Existence of residual PMMA on graphene. OM images of HGG from (A) graphene on copper foil sample, and (B) the corresponding transferred graphene on a SiO₂/Si substrate after copper etching and PMMA removal with acetone. (A color version of this figure can be viewed online.)

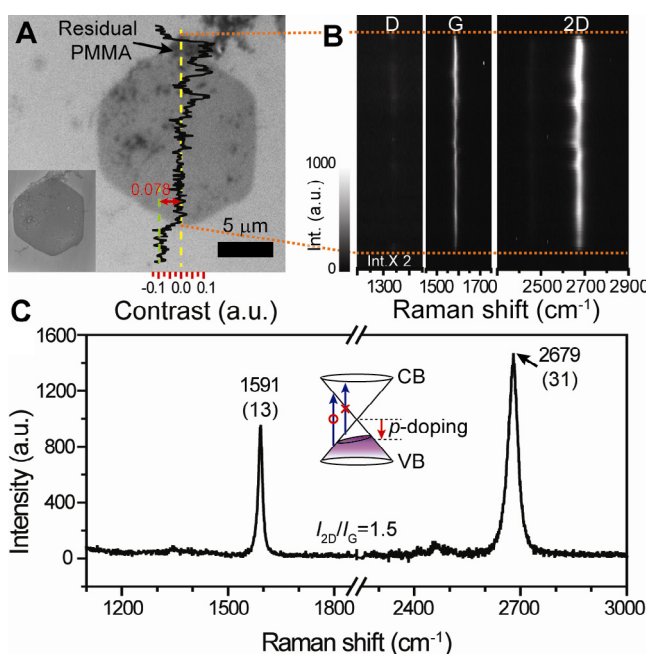


Fig. 2 – A bare supported HGG on a SiO₂/Si substrate. (A) OM image of a HGG with occasional PMMA residue shown in black. Inset: the corresponding SEM image. The optical contrast with scales (bottom) was obtained along the yellow dashed line. (B) The corresponding line Raman spectra from the D (left), G (middle), and 2D bands (right) using a 100× objective lens. The inset of (C) illustrates the Dirac cone with *p*-doping. CB and VB stand for conduction and valence bands, respectively. (A color version of this figure can be viewed online.)

convex lens (AC254-200-A-ML, $f = 200$ mm, doublet, Thorlabs) and a beam expander (1–8×, Cat. #: 68479, Edmunds) were introduced between the laser and a beam splitter to focus the excitation light into the back focal plane of an objective lens. Vertically-polarized beam parallel to edge of hexagonal graphene was introduced to sample (Fig. S2A). Calibration of Raman spectroscopy was conducted using multiple Hg/Ar lamp peaks (365.015, 404.656, 435.833, 546.074, and 579.066 nm from an Hg lamp, and 800.616, 866.794, and 912.297 nm from Ar) using a light source (HG-1, Ocean Optics)

over the entire visible range. Third-order polynomials are used to produce the wavelength linearity [26]. Si peak at 520.89 cm^{-1} was used as an internal reference, as shown in Fig. S3. Typical acquisition of micro Raman spectrum was obtained using a laser beam power below 1.3 mW and an accumulation time of 50 s to avoid laser-induced heating [29]. As in a previously-reported study [28], WFR spectroscopy can be switched from micro Raman by placing a convex lens and beam expander in the excitation path. WFR spectroscopy in the presence of the convex lens utilizes 39 mW laser power using a 100× objective lens with a collection time of 500 and 300 s for imaging and line spectra, respectively. Each of the WFR images was normalized to the background images of the substrate used. As shown in Fig. S2, placing band-pass filters corresponding to 580 and 620 nm (FB580-10 and FB620-10, respectively, FWHM = 10 nm, Thorlabs) in the emission path enables imaging of the G and 2D bands, respectively. A CCD array detector with a spectrometer can image the specific Raman bands with grating angles at 0°. By placing a kinematic slit at the focal plane in front of the spectrometer and changing the grating angle, as shown in Fig. S4, the imaging mode is converted to a line Raman spectrum mode, while the employed band pass filter is removed from the emission beam path. Typically, line Raman spectra whose center wavelengths are 547, 580, and 620 nm are collected for 300 s as Si reference, G band, and 2D band, respectively. These spectra were corrected against instrumental variations using a correction factor. To induce defect, laser irradiation using widefield illumination was applied with 50 mW for 10 h.

3. Results and discussion

Hexagonal graphene grain (HGG) was synthesized because it possesses single-domain crystallinity with a zigzag-terminated edge and minimizes the heterogeneous effect of polycrystalline graphene [23,30]. HGG growth was achieved with a low carbon feedstock via the LP-CVD method using a copper strip ($0.5 \times 4\text{ cm}^2$), according to prior method [28]. As shown in Fig. 1A, optical microscope (OM) image clearly shows HGG after oxidizing the underlying Cu strip at 160 °C for 6 min [27]. The average length of HGG was about 25 μm. The sample was transferred on 285-nm thick SiO₂/Si substrate using 75-nm thick PMMA layer. After overnight “removal” step of

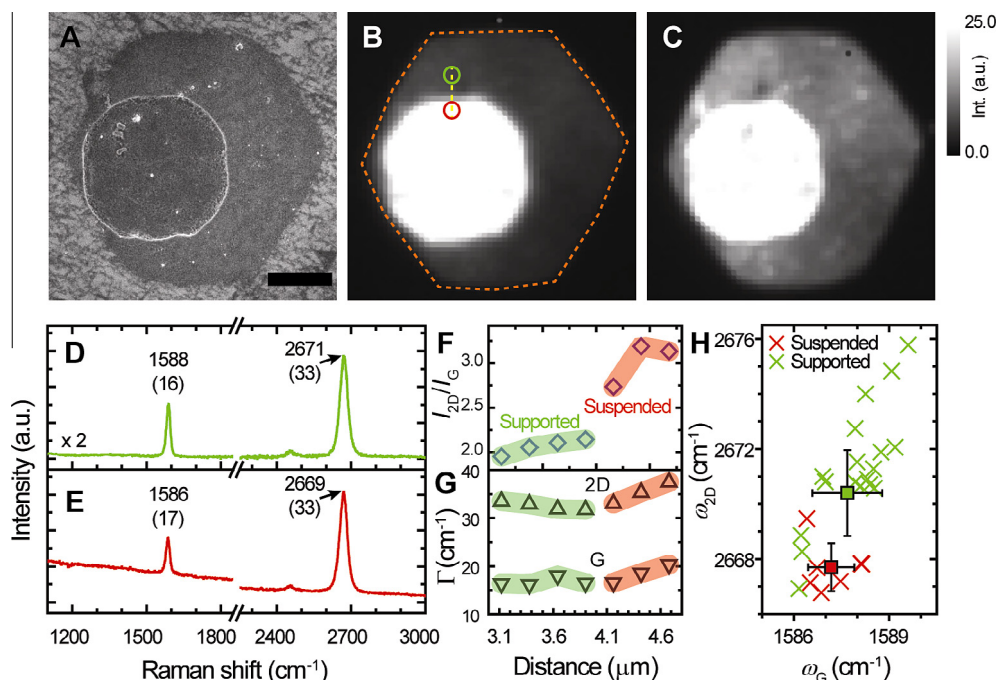


Fig. 3 – A PMMA-covered, suspended HGG grain over a well. (A) An SEM image, and the corresponding WFR images of the (B) G and (C) 2D bands. Scale bar: 3 μm . Representative Raman spectra of (D) supported, and (E) suspended graphene regions, respectively. The numbers in-plane and in the bracket note the position and FWHM of the respective bands. (F) I_{2D}/I_G ratio, and (G) FWHM (Γ) of the G and 2D bands according to the distance extracted from the yellow dashed line in (B). (H) Plot of ω_G versus ω_{2D} according to the graphene regions. (A color version of this figure can be viewed online.)

PMMA in acetone bath, the HGG sample (Fig. 1B) still exhibits PMMA residue (indicated by arrow). Pale lines devoid of PMMA are formed along Cu grain boundaries, originating from low adhesion of spuncoated PMMA layer to the recessed Cu grain boundary. The existence of PMMA was confirmed by comparing Fourier transform (FT)-infrared (IR) spectrum of the sample with that of bulk PMMA sample (Fig. S5A and B), exhibiting identical PMMA fingerprint such as 1732 cm^{-1} from C=O stretching band (see SD for detailed explanation). Utilizing an exposed and PMMA-covered HGGs, WFR spectroscopy [28] was conducted to obtain effect of PMMA on graphene with spatial and spectral information.

Bare supported HGG was first examined. HGG sample with 10- μm wide sample is clearly visible in the OM image (Fig. 2A) and scanning electron microscope (SEM) image (inset of Fig. 2A). This sample was obtained from the PMMA-uncovered region, indicated by red arrow in Fig. S5. Upon closer look, although there are remaining PMMA residues as shown in black speckle, most of HGG surface is exposed to air. In order to confirm that this is monolayer graphene, we obtained average contrast value C , which is defined by $C = (R_o - R)/R_o$, where R and R_o are the reflectance of graphene/substrate and substrate only, respectively (see Section 2). Average contrast value of PMMA-free graphene region (black trace of Fig. 2A) exhibits ~ 0.08 , in good agreement with those (i.e. 0.09) obtained from mechanically-exfoliated single-layer graphene (SLG) having the same SiO_2 thickness (i.e., 285 nm) [31]. It is noteworthy that PMMA residue also contributes to contrast value on top of that of graphene. Spatial distribution of Raman spectra was acquired using WFR along the yellow

dashed line (see Section 2 for the detailed line Raman measurement). The synthesized monolayer HGG exhibits intense 2D band near 2679 cm^{-1} compared to G band near 1591 cm^{-1} , as shown in Fig. 2B. We observed spatial variation in G and 2D band positions which did not correlate with D bands near 1345 cm^{-1} , suggesting the heterogeneity near local graphene environment. The representative Raman spectrum (Fig. 2C) exhibits G and 2D bands at 1591 and 2679 cm^{-1} , having intensity ratio of 2D over G bands (I_{2D}/I_G) with 1.5. The reason for upshifted G band position was previously ascribed to substrate-induced O_2 doping of the bare graphene [32]. As a result, p -doping of Dirac cone at K point of Brillouin zone occurs as shown in inset of Fig. 2C. Such p -doping changes bond strength of C–C bonds and leads to simultaneous G and 2D bands upshift. The optical transition in the doped state is prohibited and results in G and 2D bands stiffening. Since defect on graphene also affects G and 2D positions [33], the degree of defect as a function of intensity of D over G bands (I_D/I_G) was also probed. Fig. S6 exhibits line Raman spectra of the same line after 10 h 532-nm laser irradiation (see Section 2). Defect further upshifts ω_G and ω_{2D} by 5 and 3 cm^{-1} when I_D/I_G is 50%, which will be considered in later discussion.

Now, we probed graphene containing PMMA residue suspended over a well because suspended, PMMA-covered graphene displays phonon modes decoupled from a underlying substrate. Fig. 3A shows a SEM image of PMMA-covered HGG over a 6.7- μm wide well which was fabricated by conventional photolithography step. The corresponding G and 2D band images (Fig. 3B and C, respectively) using bandpass

filters (10 nm bandwidth, see Section 2) display spatially-varying intensities (below $\sim 35\%$ and 38% from the average values, respectively) over entire region except in the well whose intensity is much greater owing to the difference in reflectivity of the underlying substrate. The intensities of the 2D bands (Fig. 3C) are nearly two times higher than those of the G band (Fig. 3B) in the supporting region of the monolayer HGG. Raman spectrum obtained from a supported region on the substrate (Fig. 3D) exhibits G and 2D band positions (FWHM) at 1588 (16) and 2671 (33) cm^{-1} , respectively, showing an intensity of 2D over G band (I_{2D}/I_G) ratio of ~ 1.9 with no defect peak near 1345 cm^{-1} . The observed G (2D) band position is 3 (8) cm^{-1} downshifted from the bare monolayer graphene in Fig. 2, showing much larger shift in ω_{2D} as compared to ω_G . This suggests that PMMA residue makes graphene approach to the charge neutral point. Furthermore, the PMMA-covered, suspended graphene over well further downshift ω_G (ω_{2D}) by 0.5 (2.7) cm^{-1} from the supported graphene, suggesting that role of PMMA is significant on graphene.

Part F and G of Fig. 3 illustrate the spatial I_{2D}/I_G ratio and the FWHM of the G and 2D band (Γ_G and Γ_{2D} , respectively) trends. The average I_{2D}/I_G ratio increased from ~ 2.0 to ~ 2.6 from the supported to suspended regions, which can be explained by the aforementioned phonon softening of G band. In addition, while the average Γ_G and Γ_{2D} at the supported region are 16 and 33 cm^{-1} , respectively, those from the suspended region exhibit increased widths by ~ 1 and 3 cm^{-1} , respectively, supporting phonon-softening. The ω_G and ω_{2D} (Fig. 3H) from the suspended region exhibits downshift from the PMMA-covered supported graphene whose average ω_G and ω_{2D} are 1588 ± 1.1 and 2670 ± 1.6 cm^{-1} , respectively. The average position change of the 2D band ($\Delta\omega_{2D} = 7$ cm^{-1}) from supported to suspended region is more responsive than that ($\Delta\omega_G = 3$ cm^{-1}) of the G band.

In the presence or absence of residual PMMA, changes in position and width of G and 2D bands were significant. For this, defect-containing Raman spectra (i.e., $I_D/I_G > 20\%$) were carefully discarded and the spatial Raman points from various HGGs are presented in terms of respective band positions, band width, and I_{2D}/I_G ratio (Fig. 4A–C, respectively). Mean values are tabulated in Table S1 to determine the physical nature of Raman mode shifts [26]. Fig. 4A illustrates a plot of ω_G and ω_{2D} extracted from various HGGs with different environments (i.e., bare graphene/substrate, residual PMMA on graphene/substrate, and residual PMMA on graphene suspended over a well). ω_G and ω_{2D} values of charge-neutral suspended graphene value (1581 and 2667.5 cm^{-1} , respectively) from Ref. [34] are added after correction of energy dispersive ω_{2D} by excitation shift factor (i.e., 88 cm^{-1}/eV) [35]. Using this as a reference point, two $\Delta\omega_{2D}/\Delta\omega_G$ lines originating from either large-sloped strain (e_T , $\Delta\omega_{2D}/\Delta\omega_G = 2.2$ – 2.8) or low-sloped doping (e_n , $\Delta\omega_{2D}/\Delta\omega_G = 0.7$) [26,36–38] along with scales are drawn to distinguish main contribution of various HGG, as shown in Fig. 4A. Mean value of bare graphene sample on substrate positioned at 1st quadrant of two diagonal lines with distribution of correlation points along strain line. This suggests that bare CVD graphene undergoes concomitant p -doping and compressive strain, contrasted with mechanically exfoliated graphene having tensile-strain [39]. When graphene is covered with residual PMMA, the average correlation

point of the graphene is positioned at 4th quadrant, having p -doping along with tensile strain. Interestingly, doping level (i.e., $5 \times 10^{12} \text{ cm}^{-2}$) remains to that of bare graphene (Fig. 4B) along strain line (i.e. -0.1%). In addition, the strain value exerted by residual PMMA on graphene has approximately $+0.15\%$ from the bare graphene sample, suggesting tensile strain. The residual PMMA-containing graphene suspended over well further downshifts the correlation mean position along the strain line. Under this unrestricted condition, PMMA exerted more tensile strain on graphene.

We illustrate the effect of residual PMMA shown in Fig. 4A as schematics (Fig. 4B–D). Fig. 4B illustrates schematics of effect of residual PMMA on graphene. Unlike mechanically-exfoliated graphene [26], bare graphene conforms undulating SiO_2/Si substrate (top) and shows compressive strain. The SiO_2 substrate having height undulation with RMS roughness of 0.1 nm (Fig. S7) seems to facilitate oxygen doping on graphene, which exhibits pronounced p -doping concomitant with strain. In the presence of residual PMMA (Fig. 4C), graphene preferentially interacts with residual PMMA due to their similar Hildebrand solubility parameters (i.e., 22.7 and 23 $\text{MPa}^{1/2}$, respectively) [41] as compared to that of SiO_2 . As a result, graphene follows topography of residual PMMA, rather than bare graphene does SiO_2 . In addition, because residual PMMA on graphene has finite thickness over few nanometer [24], graphene would less conform the substrate and is partially suspended over the protrusions from the substrate (Fig. 4D). The fact that doping value maintains in the presence/absence of PMMA indicates that the contact between protruding SiO_2 features and graphene is main contributor to doping and PMMA has negligible effect. Similar trend has been observed in single-walled carbon nanotube (SWNT) [42–44]: while SWNT on quartz substrate does not have or weak photoluminescence (PL) [43,45], SWNT embedded in PMMA [44] or on sapphire [45] displays strong PL. This is attributed to significant doping effect of SiO_2 compared to neutral PMMA or basic sapphire. Suspended PMMA/graphene (Fig. 4D) over a well is expected to sag due to the apparent increased weight, leading to more tensile strain than that of supported case.

The FWHM of the G and 2D bands are plotted in Fig. 4E. Increasing Γ_G and Γ_{2D} values were exhibited by bare-supported, defective, PMMA-covered supported, and PMMA-covered suspended HGGs in that order, with the average Γ_G (Γ_{2D}) spanning from 17 (36) to 13 (31) cm^{-1} . The reason for line broadening is that graphene under strain splits G bands into low and high frequency modes, showing apparent mode broadening. It is noted that broadening of Γ can stem from two extreme cases: either phonon softening [46] due to C–C bond order change from extremely clean graphene or broadening due to defective graphene. In our observation, defective graphene, whose I_D/I_G ratio is greater than 20%, shows lesser broadening than that of PMMA-covered HGG does. Similar to the strain slope of the correlation band position, the slope $\Delta\Gamma_{2D}/\Delta\Gamma_G$ (i.e., 0.59) between bare and PMMA-covered SLG can be interpreted as broadening of the peak widths of the G and 2D bands as a result of strain with maintained doping level [46]. I_{2D}/I_G ratios from various HGG samples are also abridged in Fig. 4F. PMMA-covered suspended HGG exhibits a high average I_{2D}/I_G of 2.7, mainly due to the aforementioned strain effect, followed by PMMA-covered supported HGG at 2,

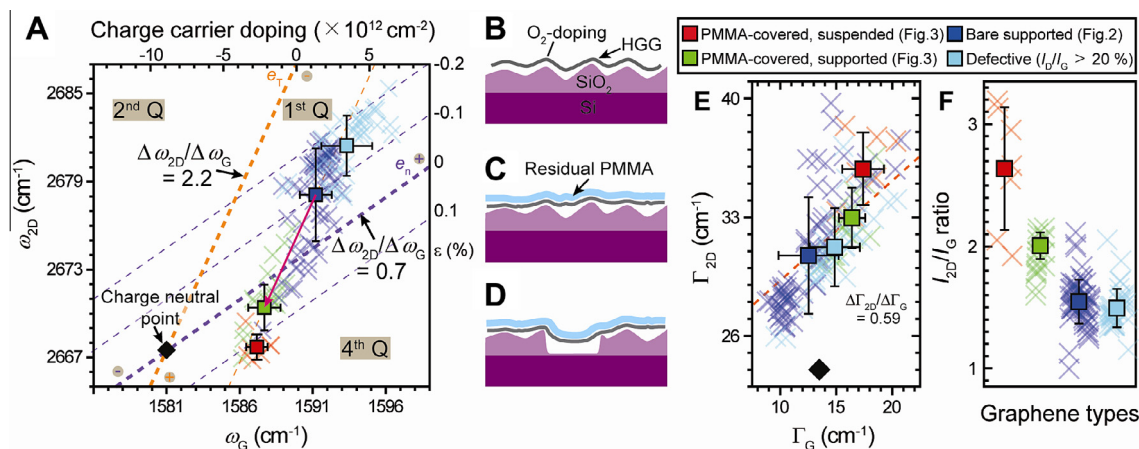


Fig. 4 – Breaking strain and doping contributions from various HGGs. (A) Correlated plot of ω_G and ω_{2D} . The red and purple dotted line indicates strain-induced (e_T) and doping-induced (e_n) position changes, obtained from Refs. [40,26]. Diamond symbol indicates charge-neutral graphene. (B–D) Schematic illustration of (B) bare HGG on SiO₂/Si substrate, (C) residual PMMA/HGG on the substrate, and (D) residual PMMA/HGG suspended over a well. (E) Plot of the G and 2D band FWHM, where the red dotted line is drawn for guidance of strain line. (F) I_{2D}/I_G ratio according to various HGG samples. (A color version of this figure can be viewed online.)

and finally bare supported graphene with the lowest average value of 1.5. The I_{2D}/I_G ratios are significantly affected by tensile strain, and defects to a lesser extent. Those I_{2D}/I_G ratios can be further calibrated with spectrometer efficiency according to each wavelength (by factor of 1.06) and polarization direction, as shown in Fig. S2A.

4. Conclusions

We have presented a systematic Raman study on synthesized HGGs with diverse PMMA and substrate environments. Complicate Raman G and 2D bands were analyzed without any thermal treatment according to position, width, and I_{2D}/I_G ratio. Mapping of the correlated G and 2D band positions reveals strain and doping contributions from various HGGs. Strong polymer-graphene interaction enables graphene adhere to residual PMMA and exhibits moderate tensile strain, as compared to compressive-strained bare graphene on substrate. In addition, graphene covered by residual PMMA maintains its doping level as similar as that of bare graphene, suggesting protruding substrate feature as main doping contributor. This study provides an explanation about role of residual PMMA with underlying graphene/substrate in terms of strain, doping, and defects.

Conflict of interest

The authors declare no conflict of interest.

Acknowledgements

The authors appreciate J. Kim for help with the contrast simulation. This research was supported by Basic Science Research Program through the National Research Foundation of Korea (NRF) funded by the Ministry of Education, Science and Technology (2014R1A1A2055572), and in part

by the Yonsei University Future-Leading Research Initiative of 2014.

Appendix A. Supplementary data

Supplementary data associated with this article can be found, in the online version, at <http://dx.doi.org/10.1016/j.carbon.2015.01.055>.

REFERENCES

- [1] Novoselov KS, Geim AK, Morozov SV, Jiang D, Katsnelson MI, Grigorieva IV, et al. Two-dimensional gas of massless dirac fermions in graphene. *Nature* 2005;438(7065):197–200.
- [2] Zhang Y, Tan Y-W, Stormer HL, Kim P. Experimental observation of the quantum hall effect and berry's phase in graphene. *Nature* 2005;438(7065):201–4.
- [3] Geim AK, Novoselov KS. The rise of graphene. *Nat Mater* 2007;6(3):183–91.
- [4] Lee C, Wei X, Kysar JW, Hone J. Measurement of the elastic properties and intrinsic strength of monolayer graphene. *Science* 2008;321(5887):385–8.
- [5] Nair RR, Blake P, Grigorenko AN, Novoselov KS, Booth TJ, Stauber T, et al. Fine structure constant defines visual transparency of graphene. *Science* 2008;320(5881):1308.
- [6] Chen S, Brown L, Levendorf M, Cai W, Ju S-Y, Edgeworth J, et al. Oxidation resistance of graphene-coated cu and cu/nl alloy. *ACS Nano* 2011;5(2):1321–7.
- [7] Bunch JS, Verbridge SS, Alden JS, van der Zande AM, Parpia JM, Craighead HG, et al. Impermeable atomic membranes from graphene sheets. *Nano Lett* 2008;8(8):2458–62.
- [8] Bae S, Kim H, Lee Y, Xu X, Park J-S, Zheng Y, et al. Roll-to-roll production of 30-inch graphene films for transparent electrodes. *Nat Nanotechnol* 2010;5(8):574–8.
- [9] Yuk JM, Park J, Ercius P, Kim K, Hellebusch DJ, Crommie MF, et al. High-resolution em of colloidal nanocrystal growth using graphene liquid cells. *Science* 2012;336(6077):61–4.

- [10] Novoselov KS, Geim AK, Morozov SV, Jiang D, Zhang Y, Dubonos SV, et al. Electric field effect in atomically thin carbon films. *Science* 2004;306(5696):666–9.
- [11] Kim KS, Zhao Y, Jang H, Lee SY, Kim JM, Kim KS, et al. Large-scale pattern growth of graphene films for stretchable transparent electrodes. *Nature* 2009;457(7230):706–10.
- [12] Li X, Cai W, An J, Kim S, Nah J, Yang D, et al. Large-area synthesis of high-quality and uniform graphene films on copper foils. *Science* 2009;324(5932):1312–4.
- [13] Berger C, Song Z, Li T, Li X, Ogbazghi AY, Feng R, et al. Ultrathin epitaxial graphite: 2d electron gas properties and a route toward graphene-based nanoelectronics. *J Phys Chem B* 2004;108(52):19912–6.
- [14] Hummers WS, Offeman RE. Preparation of graphitic oxide. *J Am Chem Soc* 1958;80(6):1339.
- [15] Hernandez Y, Nicolosi V, Lotya M, Blighe FM, Sun ZY, De S, et al. High-yield production of graphene by liquid-phase exfoliation of graphite. *Nat Nanotechnol* 2008;3(9):563–8.
- [16] Lotya M, Hernandez Y, King PJ, Smith RJ, Nicolosi V, Karlsson LS, et al. Liquid phase production of graphene by exfoliation of graphite in surfactant/water solutions. *J Am Chem Soc* 2009;131(10):3611–20.
- [17] Green AA, Hersam MC. Solution phase production of graphene with controlled thickness via density differentiation. *Nano Lett* 2009;9(12):4031–6.
- [18] Tsen AW, Brown L, Levendorf MP, Ghahari F, Huang PY, Havener RW, et al. Tailoring electrical transport across grain boundaries in polycrystalline graphene. *Science* 2012;336(6085):1143–6.
- [19] Ruiz-Vargas CS, Zhuang HL, Huang PY, van der Zande AM, Garg S, McEuen PL, et al. Softened elastic response and unzipping in chemical vapor deposition graphene membranes. *Nano Lett* 2011;11(6):2259–63.
- [20] Wang Y, Tong SW, Xu XF, Özyilmaz B, Loh KP. Interface engineering of layer-by-layer stacked graphene anodes for high-performance organic solar cells. *Adv Mater* 2011;23(13):1514–8.
- [21] Lee WH, Park J, Sim SH, Jo SB, Kim KS, Hong BH, et al. Transparent flexible organic transistors based on monolayer graphene electrodes on plastic. *Adv Mater* 2011;23(15):1752–6.
- [22] Chan J, Venugopal A, Pirkle A, McDonnell S, Hinojos D, Magnuson CW, et al. Reducing extrinsic performance-limiting factors in graphene grown by chemical vapor deposition. *ACS Nano* 2012;6(4):3224–9.
- [23] Lin Y-C, Lu C-C, Yeh C-H, Jin C, Suenaga K, Chiu P-W. Graphene annealing: how clean can it be? *Nano Lett* 2011;12(1):414–9.
- [24] Suk JW, Lee WH, Lee J, Chou H, Piner RD, Hao Y, et al. Enhancement of the electrical properties of graphene grown by chemical vapor deposition via controlling the effects of polymer residue. *Nano Lett* 2013;13(4):1462–7.
- [25] Pirkle A, Chan J, Venugopal A, Hinojos D, Magnuson CW, McDonnell S, et al. The effect of chemical residues on the physical and electrical properties of chemical vapor deposited graphene transferred to SiO_2 . *Appl Phys Lett* 2011;99(12).
- [26] Lee JE, Ahn G, Shim J, Lee YS, Ryu S. Optical separation of mechanical strain from charge doping in graphene. *Nat Commun* 2012;3:1024.
- [27] Jia CC, Jiang JL, Gan L, Guo XF. Direct optical characterization of graphene growth and domains on growth substrates. *Sci Rep* 2012;2.
- [28] Havener RW, Ju S-Y, Brown L, Wang Z, Wojcik M, Ruiz-Vargas CS, et al. High-throughput graphene imaging on arbitrary substrates with widefield Raman spectroscopy. *ACS Nano* 2011;6(1):373–80.
- [29] Cai W, Moore AL, Zhu Y, Li X, Chen S, Shi L, et al. Thermal transport in suspended and supported monolayer graphene grown by chemical vapor deposition. *Nano Lett* 2010;10(5):1645–51.
- [30] Vlasiouk I, Regmi M, Fulvio P, Dai S, Datskos P, Eres G, et al. Role of hydrogen in chemical vapor deposition growth of large single-crystal graphene. *ACS Nano* 2011;5(7):6069–76.
- [31] Ni ZH, Wang HM, Kasim J, Fan HM, Yu T, Wu YH, et al. Graphene thickness determination using reflection and contrast spectroscopy. *Nano Lett* 2007;7(9):2758–63.
- [32] Ryu S, Liu L, Berciaud S, Yu Y-J, Liu H, Kim P, et al. Atmospheric oxygen binding and hole doping in deformed graphene on a SiO_2 substrate. *Nano Lett* 2010;10(12):4944–51.
- [33] Martins Ferreira EH, Moutinho MVO, Stavale F, Lucchese MM, Capaz RB, Achete CA, et al. Evolution of the Raman spectra from single-, few-, and many-layer graphene with increasing disorder. *Phys Rev B* 2010;82(12):125429.
- [34] Berciaud S, Ryu S, Brus LE, Heinz TF. Probing the intrinsic properties of exfoliated graphene: Raman spectroscopy of free-standing monolayers. *Nano Lett* 2008;9(1):346–52.
- [35] Mafra DL, Samsonidze G, Malard LM, Elias DC, Brant JC, Plentz F, et al. Determination of I_a and I_{2D} phonon dispersion relations of graphene near the Dirac point by double resonance Raman scattering. *Phys Rev B* 2007;76(23):233407.
- [36] Metzger C, Rémi S, Liu M, Kusminskiy SV, Castro Neto AH, Swan AK, et al. Biaxial strain in graphene adhered to shallow depressions. *Nano Lett* 2009;10(1):6–10.
- [37] Ding F, Ji H, Chen Y, Herklotz A, Dörr K, Mei Y, et al. Stretchable graphene: a close look at fundamental parameters through biaxial straining. *Nano Lett* 2010;10(9):3453–8.
- [38] Mohiuddin TMG, Lombardo A, Nair RR, Bonetti A, Savini G, Jalil R, et al. Uniaxial strain in graphene by Raman spectroscopy: G peak splitting, Grüneisen parameters, and sample orientation. *Phys Rev B* 2009;79(20):205433.
- [39] Bao W, Miao F, Chen Z, Zhang H, Jang W, Dames C, et al. Controlled ripple texturing of suspended graphene and ultrathin graphite membranes. *Nat Nanotechnol* 2009;4(9):562–6.
- [40] Das A, Chakraborty B, Piscanec S, Pisana S, Sood AK, Ferrari AC. Phonon renormalization in doped bilayer graphene. *Phys Rev B* 2009;79(15):155417.
- [41] Hernandez Y, Lotya M, Rickard D, Bergin SD, Coleman JN. Measurement of multicomponent solubility parameters for graphene facilitates solvent discovery. *Langmuir* 2009;26:3208–13.
- [42] Lee D, Ahn G, Ryu S. Two-dimensional water diffusion at a graphene-silica interface. *J Am Chem Soc* 2014;136(18):6634–42.
- [43] Xie L, Liu C, Zhang J, Zhang Y, Jiao L, Jiang L, et al. Photoluminescence recovery from single-walled carbon nanotubes on substrates. *J Am Chem Soc* 2007;129(41):12382–3.
- [44] Ai N, Walden-Newman W, Song Q, Kalliakos S, Strauf S. Suppression of blinking and enhanced exciton emission from individual carbon nanotubes. *ACS Nano* 2011;5(4):2664–70.
- [45] Kiowski O, Lebedkin S, Hennrich F, Kappes MM. Single-walled carbon nanotubes show stable emission and simple photoluminescence spectra with weak excitation sidebands at cryogenic temperatures. *Phys Rev B* 2007;76(7):075422.
- [46] Huang M, Yan H, Chen C, Song D, Heinz TF, Hone J. Phonon softening and crystallographic orientation of strained graphene studied by Raman spectroscopy. *PNAS USA* 2009;106(18):7304–8.

Role of Residual Polymer on Chemical Vapor Grown Graphene by Raman Spectroscopy

Eunhye Koo and Sang-Yong Ju*

Department of Chemistry, Yonsei University, Seoul 120-749, Republic of Korea

* Correspondence E-mail: syju@yonsei.ac.kr

Table of contents	S1
Figure S1. Photograph of a custom CVD setup.....	S2
1. Photolithography of Si substrate	S2
Figure S2. (A) Schematic optical setup of micro/wide-field Raman spectroscope and (B) Polarization dependency of the grating.....	S3
Figure S3. Slit size and laser power dependence of 520.89 cm^{-1} Si peak.....	S4
Figure S4. Schematic procedure for wide-field Raman images and line Raman spectra.....	S4
2. IR comparison	S5
Figure S5. (A) OM image of PMMA-free region from PGGs on a substrate and (B) Comparison of fourier transform (FT)-IR spectra depending on the existence of PMMA.....	S5
Figure S6. Line Raman spectra and plot of G (ω_G) vs. 2D band positions (ω_{2D}) from PGG in Fig. 2 after laser irradiation.....	S6
Table S1. Average positions, FWHMs, and I_{2D}/I_G ratios obtained from various graphene grains.....	S6
Figure S7. (A) AFM height topography of a bare 285-nm thick SiO_2/Si substrate. (B) The corresponding height variations according to positions.	S7

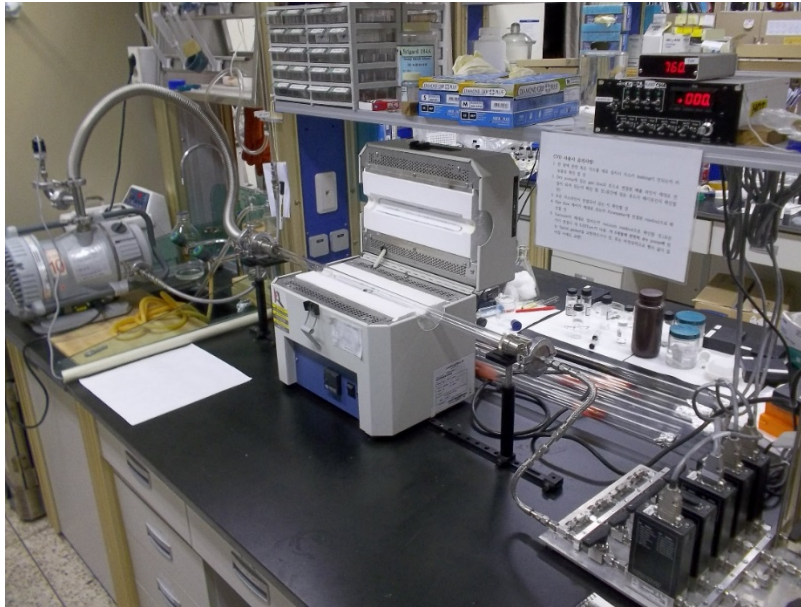


Figure S1. Photograph of custom-made CVD setup.

1. Photolithography of Si substrate.

4-inch diameter, 285 nm-thick SiO₂/Si substrate (Lot#7400383-603-Z, degenerately *p*-doped, resistivity = 1-10 Ω-cm, Shinetsu, Japan) was utilized throughout this study unless otherwise noted. The photoresist (PR, Cat. #: AZ GXR601, AZ Electronic Materials) was spun-coated at 1500 rpm for 85 sec on the Si substrate to produce 1.2 μm-thick photoresist layer. The photoresist-covered Si substrate was post-baked for 90 sec at 110 °C and subsequently patterned by a contact mask aligner (MA6, Suss MacroTec, Germany). The patterned substrate was further developed with a diluted tetramethylammonium hydroxide (TMAH) solution (MIF300, AZ Electronic Materials). Reactive ion etcher (RB4510, LAM Research) using fluorinated gas was utilized to etch away SiO₂ on Si substrate with desired hole depth.

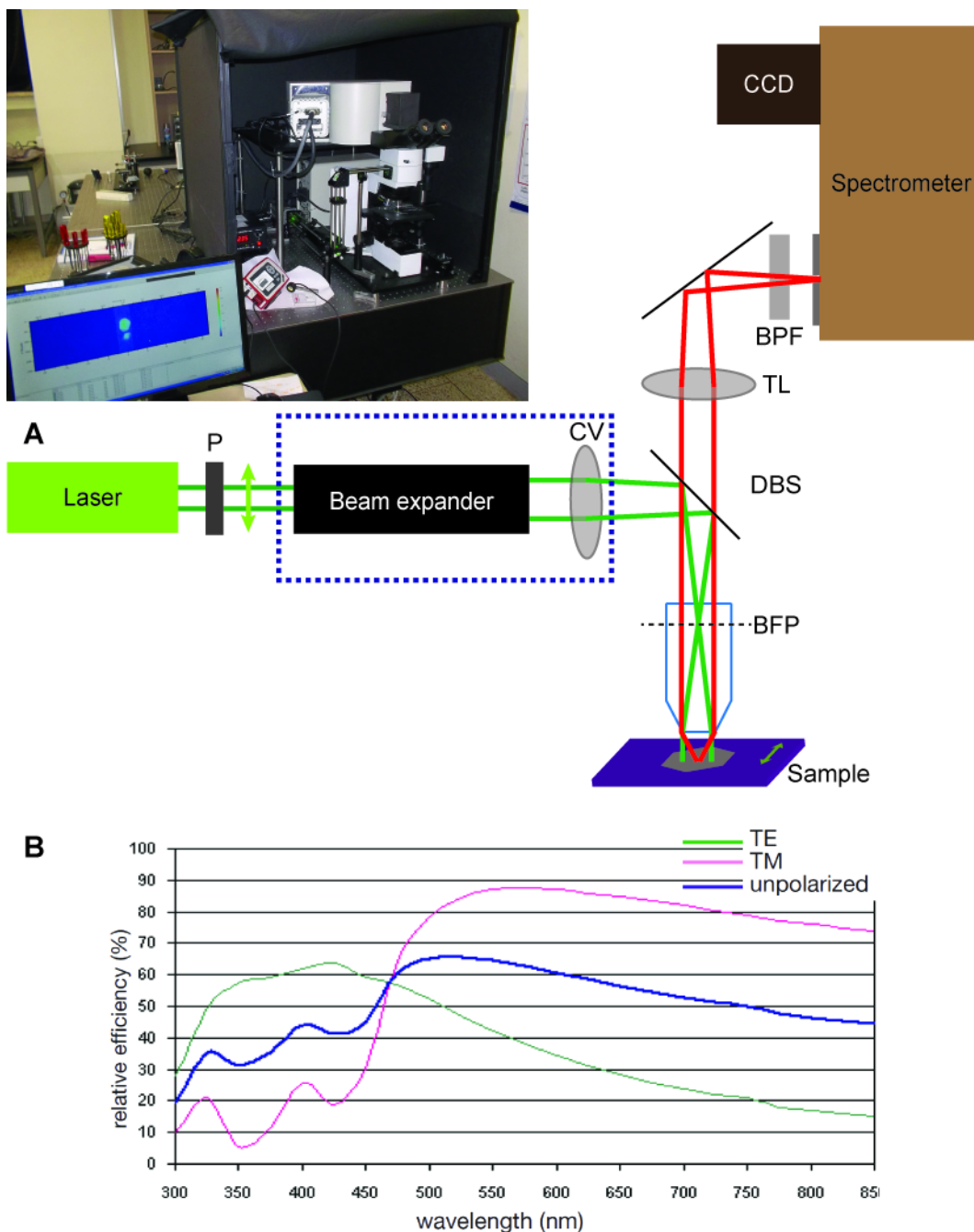


Figure S2. (A) Schematic optical setup of micro/wide-field Raman spectroscope. The inset shows a photograph of the installed Raman setup. The green and red lines represent excitation and emission paths, respectively. The green arrow indicates vertical polarization direction. Notation for abbreviation: P: polarizer, CV: convex lens, DBS: dichroic beam splitter, BFP: back focal plane, TL: tube lens, and BPF: band pass filter. Optical components with a dashed box are removed for micro Raman measurement. (B) Polarization dependency of the grating used in this study.

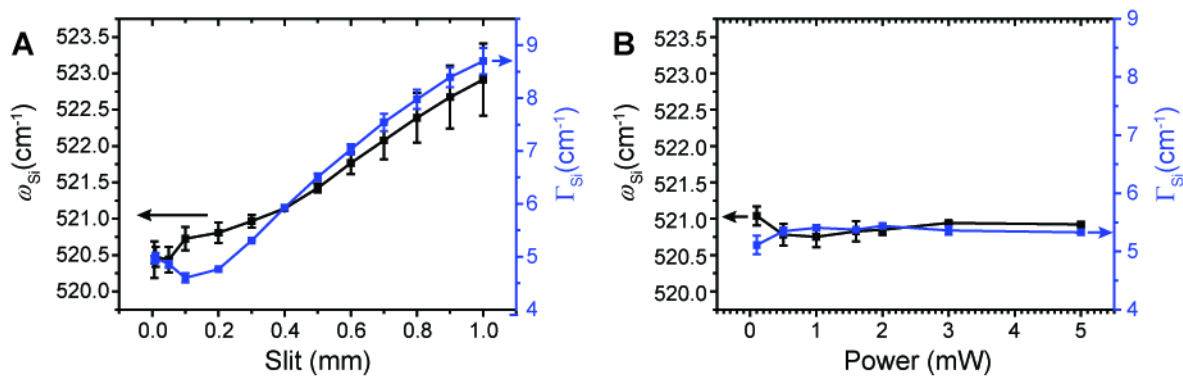


Figure S3. (A) Kinematic slit size dependence with a laser power of 1.7 mW, and (B) laser power dependence of the 520.89 cm^{-1} Si peak.

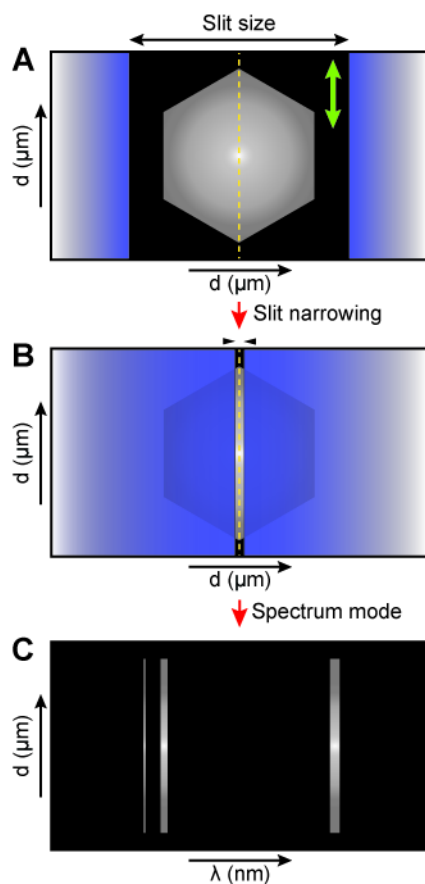


Figure S4. Schematic procedure for obtaining (A) wide-field Raman images, (B) slit narrowing operated by 0° grating angle, and (C) the corresponding line Raman spectra with appropriate grating angle along the slit. The green arrow in (A) indicates polarization direction.

2. IR comparison

IR spectra were acquired from three samples: PMMA spin-coated on a SiO₂/Si layer 285-nm in thickness, residual PMMA on graphene on the substrate, and the bare substrate. IR spectra from spin-coated PMMA on the substrate displays vibrational bands at 2928, 2861, 1732, 1448, and 1375 cm⁻¹. Bands at 2928 and 2861 cm⁻¹ originate from the symmetric and asymmetric C–H stretching mode of the –CH₂– group. The 1732 cm⁻¹ band is due to the stretching vibration of the C=O ester group. The 1448 and 1375 cm⁻¹ bands are C–H bending modes of the –CH₃ group. As a whole, the aforementioned assignment is attributed to PMMA. These PMMA signals are obtained from the residual PMMA/graphene/substrate sample, while the control substrate does not exhibit any IR features originating from PMMA.

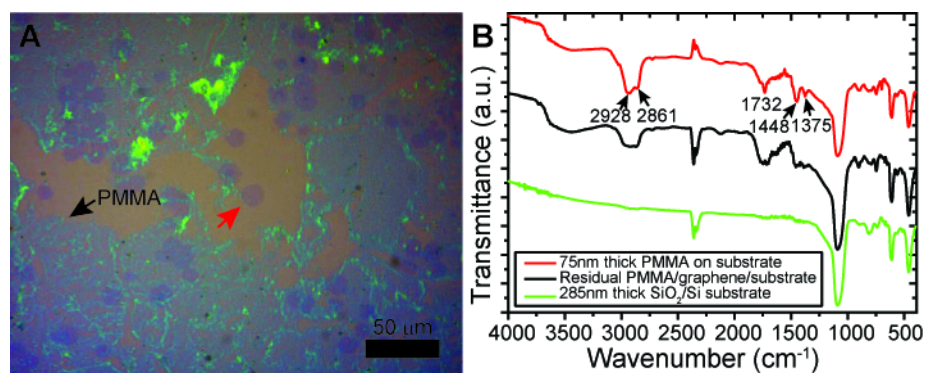


Figure S5. (A) OM image of the PMMA-free region from PGGs on a substrate. The red arrow indicates the graphene hexagon from Fig. 2. (B) Comparison of fourier transform (FT)-IR spectra of spin-coated PMMA on a SiO₂/Si substrate (red trace), residual PMMA/graphene on a substrate after acetone washing with copious amounts (black trace), and bare silicon substrate (green trace). Each spectrum is offset from top spectra for clarity.

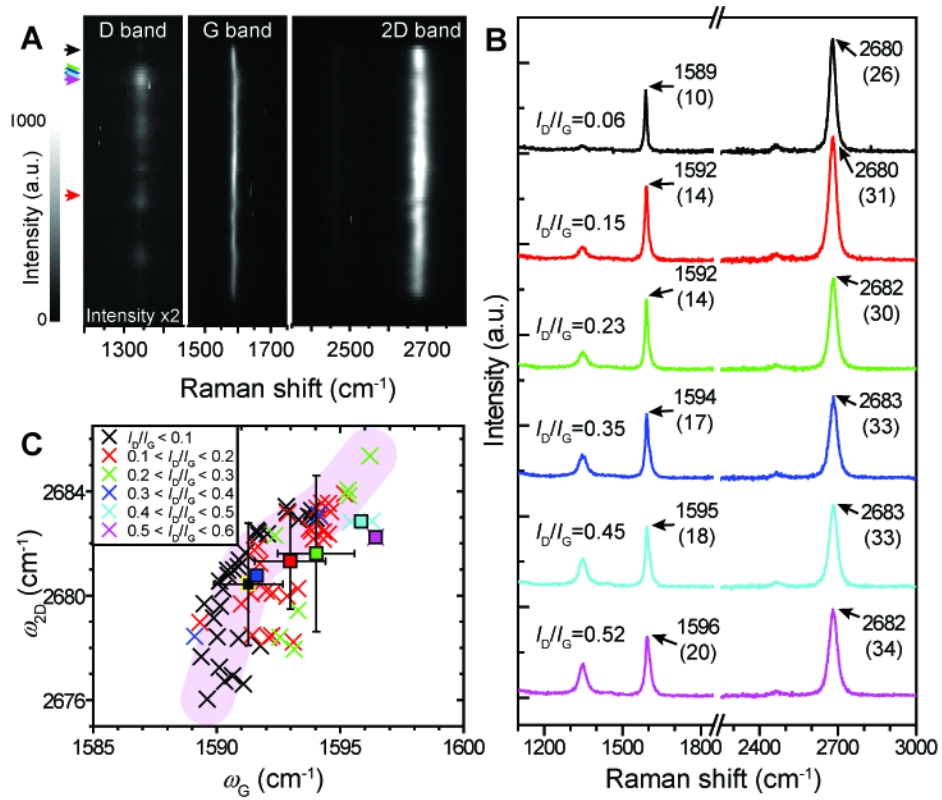


Figure S6. PMMA-free defective hexagonal graphene grain on a substrate obtained *via* prolonged laser irradiation. (A) The corresponding line Raman spectrum from the D (left), G (middle) and 2D bands (right). Note that the left side has color-coded arrows for the following Raman spectra. (B) The respective defect-derived Raman spectra. (C) Plot of ω_G vs. ω_{2D} in terms of increasing I_D/I_G values with 0.1 intervals. Standard deviation is presented with the exception of 0.4–0.6 I_D/I_G ratios, whose data points are less than 3.

Table S1. Average positions, FWHMs, and I_{2D}/I_G ratios obtained from various graphene grains.

Types of graphene grain	ω_G (cm ⁻¹)	ω_{2D} (cm ⁻¹)	Γ_G (cm ⁻¹)	Γ_{2D} (cm ⁻¹)	I_{2D}/I_G
PMMA-covered suspended	1587.2 ± 0.7	2667.7 ± 0.9	17.4 ± 1.9	35.8 ± 2.1	2.6 ± 0.5
PMMA-covered supported	1587.7 ± 1.1	2670.4 ± 1.6	16.4 ± 1.2	33.0 ± 1.8	2.0 ± 0.1
Bare supported	1591.2 ± 1.1	2678.1 ± 3.2	12.5 ± 2.7	30.7 ± 3.4	1.5 ± 0.2
Defective ($I_D/I_G > 20\%$)	1593.3 ± 1.7	2681.4 ± 2.0	14.9 ± 2.2	31.2 ± 2.3	1.5 ± 0.2

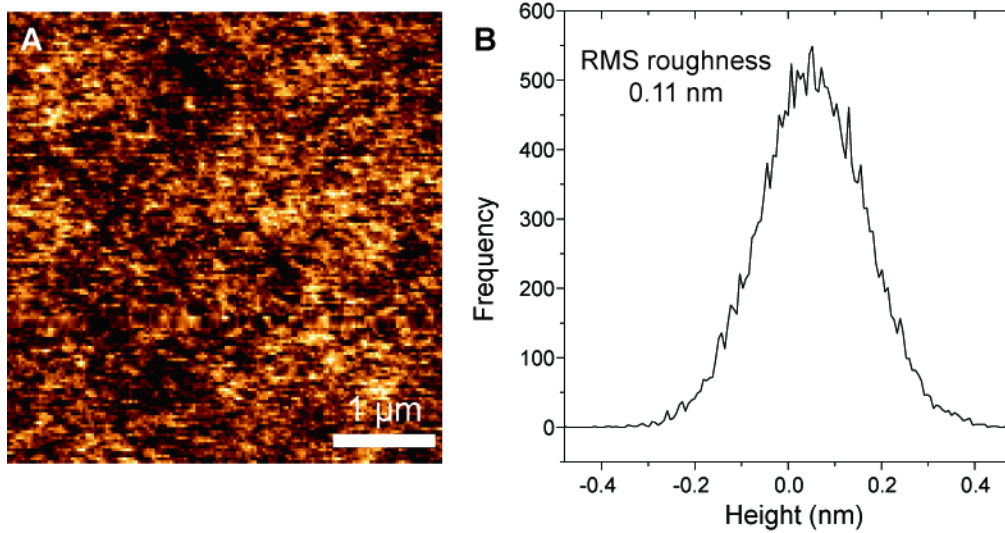


Figure S7. (A) AFM height topography of a bare 285-nm thick SiO₂/Si substrate. (B) The corresponding height variations according to positions.